JOINT X-RAY AND OPTICAL MEASUREMENTS OF THE MASS DISTRIBUTION OF THE DISTANT GALAXY CLUSTER Cl J0152.7−1357

ZHI-YING HUO,[1] SUI-JIAN XUE,[1] HAIGUANG XU,[2] GORDON SQUIRES,[3] AND PIERO ROSATI[4]

ABSTRACT

We present joint X-ray and optical observations of the high-redshift ($z \simeq 0.83$) lensing cluster Cl J0152.7−1357 made with the *Chandra X-Ray Observatory* and the Keck telescope. We confirm the existence of significant substructure at both X-ray and optical wavelengths in the form of two distinct clumps, whose temperatures are $6.6^{+2.4}_{-1.5}$ and $5.7^{+2.9}_{-1.6}$ keV, respectively. The X-ray surface brightness profiles of the two clumps can be fitted by either a single β-model or an NFW-like profile, the latter giving better fits to the central regions. We find that the X-ray–derived mass of this cluster is in good agreement with independent lensing measurements. While its appearance indicates that the cluster has not reached a dynamical equilibrium state, its X-ray luminosity L_X, temperature T, and dynamical mass M are consistent with the well-defined L_X-T and M-T relations for low-redshift galaxy clusters, which suggests that the dynamical properties of the clusters have remained almost unchanged since $z \approx 0.8$.

Key words: cosmology: observations — galaxies: clusters: general — galaxies: clusters: individual (Cl J0152.7−1357) — gravitational lensing — X-rays: galaxies

1. INTRODUCTION

Clusters of galaxies are the largest gravitationally bound systems in the universe, and they are recently formed in the hierarchical clustering scenario. Among them, massive clusters at high redshifts are of particular interest, being the most sensitive probes of the formation and evolution of cosmic structures. Robust constraints on models of structure formation and underlying cosmological parameters can be obtained through accurate X-ray measurements of the density, temperature, and metallicity of the intracluster medium (ICM; e.g., Bahcall & Cen 1992; Oukbir & Blanchard 1997; Haiman, Mohr, & Holder 2001), as well as from studies of their scaling relation, involving, for example, X-ray temperature, luminosity, and total mass. In distant clusters where lensing effects are observed, one has the ability of comparing the mass distribution derived by the X-ray data with that inferred by the lensing analysis (e.g., Tyson, Valdes, & Wenk 1990; Kaiser & Squires 1993), which is independent of the dynamical equilibrium assumption, thus testing the systematics inherent in both methodologies. Cl J0152.7−1357 is an irregular, lensing cluster with apparent substructures. The X-ray emission from its hot ICM was first detected with the *Einstein* IPC in 1980. Because of its complex morphology, the source was not formally identified as a cluster in the *Einstein* Extended Medium-Sensitivity Survey (EMSS). This same source was easily discovered as an extended source in serendipitous cluster surveys based on *ROSAT* PSPC archival data, namely, the *ROSAT* Deep Cluster Survey (RDCS; Rosati et al. 1998), the

Wide Angle *ROSAT* Pointed Survey (WARPS; Ebeling et al. 2000), and the Serendipitous High-Redshift Archival *ROSAT* Cluster Survey (SHARC; Romer et al. 2000), and it was optically identified as one of the richest and most X-ray–luminous distant clusters at $z > 0.8$. Cl J0152.7−1357 was observed with *BeppoSAX* in 1998 (Della Ceca et al. 2000, hereafter D00). The authors reported an average gas temperature of $kT = 6.46^{+1.74}_{-1.19}$ keV and a metallicity of $A = 0.53^{+0.29}_{-0.24}$ times the solar value. However, these results need to be confirmed, because the *BeppoSAX* spectrum may have been polluted by background/foreground sources that cannot be distinguished from the diffuse X-rays of the cluster itself as a result of the relatively poor spatial resolution provided by *BeppoSAX*.

Using *Chandra* data, Maughan et al. (2003) resolved Cl J0152.7−1357 into two massive subclusters, finding their temperatures to be $5.5^{+0.9}_{-0.8}$ and $5.2^{+1.1}_{-0.9}$ keV, respectively. They suggested that the cluster was in process of merging. In this paper we present a joint study combining the same *Chandra* data set with deep optical imaging data obtained with the Keck telescope. We evaluate and compare independent X-ray and lensing mass estimates. In § 2 we describe the observations and data reduction. In § 3 we present analysis of the X-ray and optical data, respectively, and we investigate and compare the different methods of mass determination. In §§ 5 and 6 we summarize and discuss these results.

Throughout the paper we adopt $H_0 = 65$ km s^{-1} Mpc^{-1}, $\Omega_m = 0.35$, and $\Omega_\Lambda = 0.65$. Thus, $1'$ at the distance of the source corresponds to 479.8 kpc. All uncertainties are quoted at the 90% confidence level unless otherwise mentioned.

2. OBSERVATIONS AND DATA REDUCTIONS

2.1. *X-Ray Observations with the Chandra Observatory*

Cl J0152.7−1357 was observed with the *Chandra* ACIS instrument for 36.5 ks on 2001 September 8. CCD chips I0–I3 and S2–S3 were operated in timed exposure mode, and the data stream was telemetered in faint mode. Diffuse X-ray emission

[1] National Astronomical Observatories, Chinese Academy of Sciences, Beijing 100012, China; hzy@bao.ac.cn.
[2] Department of Physics, Shanghai Jiao Tong University, 1954 Huashan Road, Shanghai 200030, China.
[3] *SIRTF* Science Center, California Institute of Technology, Pasadena, CA 91125.
[4] European Southern Observatory, Karl-Schwarzschild-Strasse 2, D-85748 Garching, Germany.

Filter	$t_{\exp}$ (s)	Seeing (arcsec)
B...............	7189	1.18
V...............	1500	0.87
R...............	12993	0.80
I...............	1885	0.67

with two X-ray clumps, spatially coincident with two galaxy overdensities in the optical image, were clearly detected on the I3 chip. The spectra and images analyzed in this work were all obtained with this chip.

We followed the standard procedure by using the CIAO 2.3 package to reduce the data. We excluded those data acquired during a short period (0.4 ks) when the occurrence of flares raised the background count rate to more than 1.2 times the mean value. We cleaned the event file for bad pixels and then filtered it with the standard *ASCA* grades (G 02346). This left about 36.1 ks of screened data for imaging and spectral analysis.

Twelve pointlike sources were detected using the tool WAVDETECT packaged in CIAO 2.3 and were excluded from the analysis of the diffuse X-ray emission. A comparison of X-ray and optical positions of five pointlike sources embedded in the X-ray halo of the cluster shows that the astrometric accuracy is better than $1\farcs0$, with no need of registration. We estimate that the background- and point source–subtracted 0.3–10 keV count rate of the cluster is 0.077 ± 0.006 counts s^{-1} with a $4'$ aperture. In the same band the contribution of the embedded pointlike sources is 0.023 ± 0.001 counts s^{-1}.

2.2. *Optical Observations with the Keck Telescope*

Cl J0152.7−1357 was observed with the Keck telescope as a part of a program to image high-z galaxy clusters drawn from the RDCS (Rosati et al. 1995, 1998). The operating detector was the Low Resolution Imaging Spectrograph (LRIS; Oke et al. 1995) at Cassegrain focus, with a Tektronix 2048×2048 CCD ($0\farcs215$ pixel^{-1}).

The strategy of the observations was to obtain $\simeq 3$ hr integrations in the R band in subarcsecond seeing conditions. The depth of the R-band observations was set by the goal of obtaining a sufficiently high surface density of faint, distant galaxies to allow a significant detection of weak gravitational lensing shear by a massive cluster. When the seeing conditions deteriorated or the observations were affected by the Moon, we switched to B-/V- and I-band observations, respectively. A summary of the observations is given in Table 1.

The image processing and lensing analysis followed the standard techniques described below. The two-amp mode was used and a second-order Legendre polynomial was fitted to the overscan region for each amplifier on an image-by-image basis. A median bias was created from each night's observations (comprising of 10 exposures) and subtracted from each overscan-corrected image. We created a median superflat by using all of our science observations on each night to correct for pixel-to-pixel variations in the response of the CCD.

Each individual exposure was corrected for optical distortion before creating the final, co-added image as follows. A set of stars common to our images and those of Digital Sky Survey was selected, and a second-order spatial transformation

applied, to bring our images into an orthographically projected astrometric frame. The final median image was then created by stacking the transformed images.

Our object detection and analysis technique is based on that developed by Kaiser, Squires, & Broadhurst (1995, hereafter KSB). For gravitational lensing analyses, there have been several investigations to determine the optimal method for measuring galaxy shapes, correcting for non-gravitational shape distortions, and calibrating gravitational shear estimates from galaxy shape data (e.g., KSB with extensions developed by Hoekstra et al. 1998; Luppino & Kaiser 1997; Kuijken 1999; Kaiser 2000). For ground-based data and the relatively small PSF encountered here, the standard KSB+Luppino/Kaiser (LK) algorithm is adequate for correcting point-spread function anisotropies and for the losses due to seeing and pixelization.

3. ANALYSIS OF THE *CHANDRA* DATA

3.1. *X-Ray Morphology and Pointlike Sources*

Both the previous X-ray studies and our optical observations as reported below indicate that Cl J0152.7−1357 has a complex morphology exhibiting two major concentrations. This is clearly visible in the *Chandra* broadband (0.3–10 keV) image (Fig. 1). This image has been corrected for exposure and smoothed using the CIAO tool CSMOOTH, with a minimum significance of 3 and a maximum significance of 5. The diffuse X-ray emissions cover a $1\farcm9 \times 1\farcm2$ (0.9×0.6 Mpc^2) region, with two clear peaks at R.A. = $01^h52^m44\fs1$, decl. = $-13°57'22\farcs3$ (J2000.0; northeastern clump) and R.A. = $01^h52^m39\fs7$, decl. = $-13°58'30\farcs1$ (J2000.0; southwestern clump), respectively. The projected distance between the peaks is about $1\farcm5$ (0.7 Mpc). Both clumps are reasonably symmetrically shaped and only slightly elongated in the northeast-southwest direction. This suggests that the cluster is in a
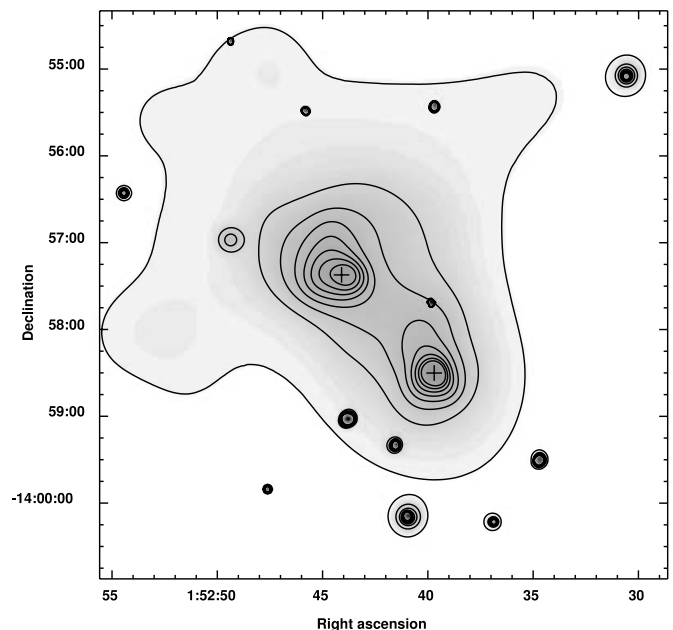

FIG. 1.—Smoothed and exposure-corrected *Chandra* image of Cl J0152.7−1357 in 0.3–10 keV band. Contours span the range: 3.6×10^{-9} to 1.5×10^{-8} photons cm^{-2} s^{-1} pixel^{-2} using a logarithmic scale. The two crosses mark the two X-ray peaks. The field of view is $6\farcm56 \times 6\farcm56$, or 3.1×3.1 Mpc^2.
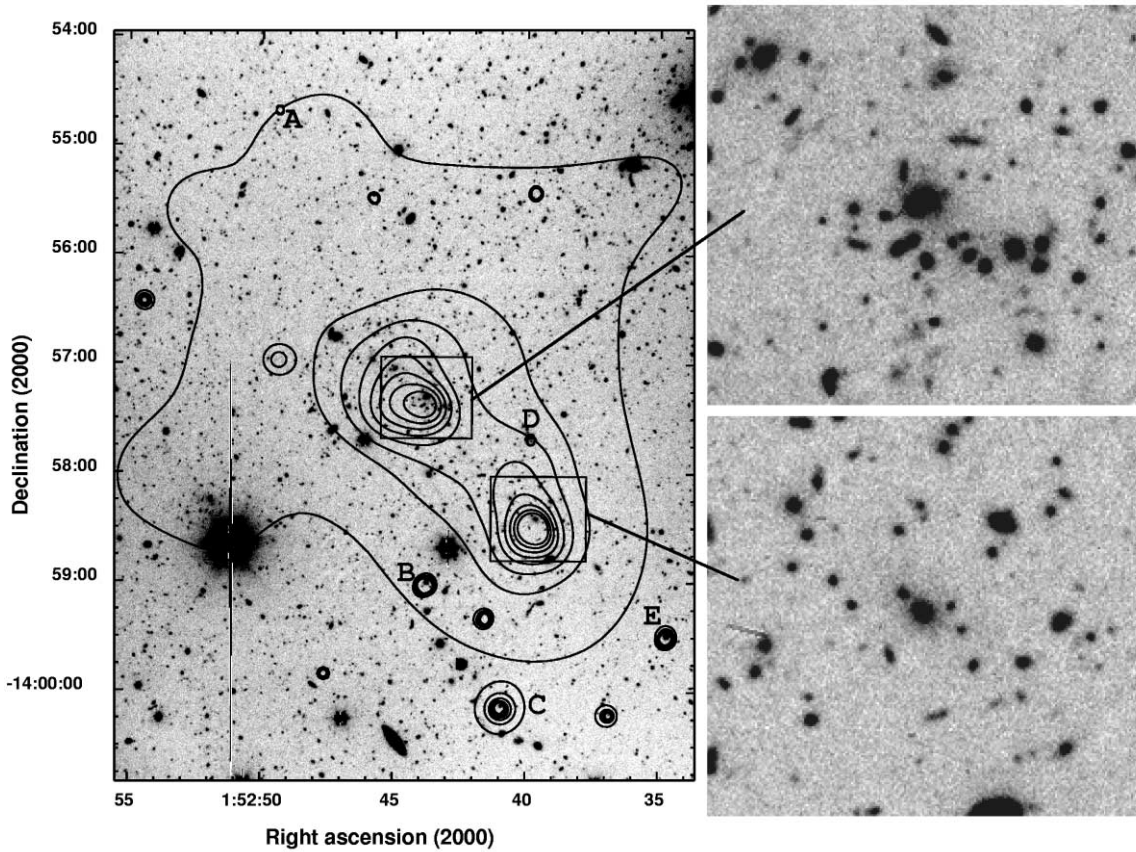
Fig. 2.—*R*-band image of Cl J0152.7−1357 obtained with the LRIS instrument at the Keck telescope with a 4 ks exposure. *Chandra* X-ray contours are overlaid (*left*). Blowup of the two cores in the Keck image (*right*).

premerger state. The northeastern clump is larger in extension but less luminous than the southwestern clump.

In Figure 2 we show the *R*-band image obtained with the Keck telescope in a 4 ks exposure, on which the *Chandra* X-ray intensity contours are overlaid in logarithmic scales, and a blowup of the two cores in the Keck image, with possible strong lensing features around the northeastern and southwestern clumps visible in the deep Keck images. In the *R* band the spatial distribution of galaxies also shows two similar concentrations. However, we notice that the optical peaks do not exactly coincide with the X-ray peaks. The offsets are 6″.0 and 4″.9 for the northeastern and southwestern clumps, respectively. This further supports the conjecture that the cluster is not in a dynamical equilibrium state and may be undergoing a merger.

A close inspection of the *Chandra* and Keck images shows a third X-ray faint clump to the east of the major structure, just north of a bright star. An overdensity of galaxies as red as those in the two main clumps is apparent in the Keck color images.

Optical counterparts of the five embedded X-ray pointlike sources have also been identified (Table 2 and Fig. 2). These sources are too faint to allow a study of their X-ray spectra, and we therefore calculate their hardness ratios defined as $H = (C_H - C_S)/(C_H + C_S)$, where C_S and C_H are the net counts in 0.3–1.5 and 1.5–7 keV, respectively. We find that the obtained hardness ratios differ greatly, inferring that these sources are of different origins. Besides their optical positions, no further information about the optical or radio counterparts of these pointlike sources was found in the literature or on-line databases.

TABLE 2
Positions, Counts, and Hardness Ratios of the Five Pointlike Sources with Optical Counterparts Embedded in the Diffuse X-Ray Emission

	Source Position (J2000.0)		Counts		
Sources	R.A.	Decl.	0.3−1.5 keV	1.5−7 keV	Hardness Ratios
A....................	01 52 45.8	−13 55 29.2	11.4 ± 3.5	5.0 ± 2.2	−0.39 ± 0.06
B....................	01 52 43.8	−13 59 02.2	216.0 ± 14.7	98.3 ± 10.0	−0.37 ± 0.01
C....................	01 52 40.9	−14 00 09.1	31.8 ± 6.1	14.7 ± 4.1	−0.37 ± 0.04
D....................	01 52 39.8	−13 57 41.5	82.3 ± 9.2	149.0 ± 12.4	0.29 ± 0.01
E....................	01 52 34.7	−13 59 29.7	23.3 ± 5.1	20.3 ± 4.8	−0.07 ± 0.01

Note.—Units of right ascension are hours, minutes, and seconds, and units of declination are degrees, arcminutes, and arcseconds.

| | Counts | | |
CLUMPS	0.5–2 keV	2–8 keV	HARDNESS RATIOS
Entire cluster	908.1 ± 32.6	264.5 ± 23.6	−0.55 ± 0.02
Northeastern clump	551.2 ± 25.3	164.5 ± 18.3	−0.54 ± 0.02
Southwestern clump	356.9 ± 20.1	100.0 ± 13.8	−0.56 ± 0.03

3.2. Spectral Fits

We extracted the 0.5–8 keV spectra and analyzed them with XSPEC (v11.2.0; Arnaud 1996) software. Background spectra were extracted from sourcefree regions adjacent to the cluster on the ACIS I3 chip. Corrections for the degradation of the quantum efficiency at low energies were made. We also computed hardness ratios for the entire cluster and the two clumps separately. The hardness ratios were defined in the same way as in § 3.1, except that the soft and hard bands were chosen this time to be 0.5–2 and 2–8 keV, respectively. We find that the hardness ratios of the two clumps are consistent with each other, suggesting a similar temperature (Table 3).

The entire cluster.—We extracted the global spectrum of the entire cluster by combining two circular regions, one centered at the peak of each clump. We fitted the combined spectrum with the absorbed MEKAL model designed for photoelectric absorbed emission emitted from isothermal gas in collisional equilibrium. In the spectral fits, we fixed the column density of the neutral hydrogen to the Galactic value (1.55×10^{20} cm^{-2}; Dickey & Lockman 1990). The observed spectrum and the best-fit model are showed in Figures 3 and 4 and Table 4, where results from previous work are also listed for comparison. The best-fit gas temperature is $6.5^{+1.7}_{-1.3}$ keV, or $6.2^{+1.6}_{-1.1}$ keV if the ICM abundance is fixed at 0.3 of the solar value. With our best-fit model, we estimate that the unabsorbed flux in 0.5–2 keV is $f_{0.5-2\mathrm{keV}} = 1.27^{+0.10}_{-0.11} \times 10^{-13}$ ergs cm^{-2} s^{-1}, corresponding to an isotropic 0.5–2 keV luminosity of $L_X = 3.50^{+0.29}_{-0.30} \times 10^{44}$ ergs s^{-1}. In the 2–10 keV band the unabsorbed flux and luminosity are $f_{2-10\mathrm{keV}} = 1.43^{+0.12}_{-0.13} \times 10^{-13}$ ergs cm^{-2} s^{-1} and $L_X = 6.30^{+0.52}_{-0.56} \times 10^{44}$ ergs s^{-1}, respectively.

The measured *Chandra* temperature is consistent with the *ROSAT* and *BeppoSAX* measurements (D00), while the calculated X-ray fluxes are lower by 42% and 38% than those obtained with *ROSAT* ($f_{0.5-2\mathrm{keV}} = 2.2 \pm 0.2 \times 10^{-13}$ ergs
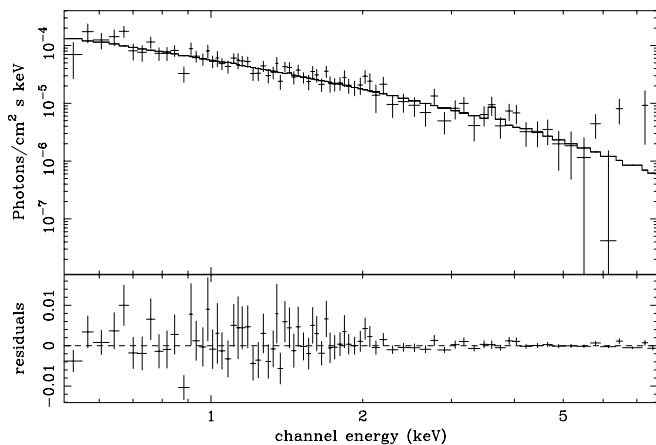
cm^{-2} s^{-1}) and *BeppoSAX* ($f_{2-10\mathrm{keV}} = 2.3 \pm 0.5 \times 10^{-13}$ ergs cm^{-2} s^{-1}), respectively. We found that the difference is primarily caused by contamination from embedded pointlike sources that were not subtracted in the previous analyses. We then estimate the contribution of pointlike sources by fitting their global spectrum with the same model as the cluster (to compare with the results from *ROSAT* and *BeppoSAX*) and find their unabsorbed flux is $f_{0.5-2\mathrm{keV}} = 6.6^{+0.7}_{-0.7} \times 10^{-14}$ ergs cm^{-2} s^{-1} and $f_{2-10\mathrm{keV}} = 9.2^{+0.7}_{-0.7} \times 10^{-14}$ ergs cm^{-2} s^{-1}. Therefore, the sum of flux from the cluster and pointlike sources from the *Chandra* data is consistent with the *ROSAT* and *BeppoSAX* measurements.

The two clumps.—We extracted the spectra of the two clumps separately from circular regions centered on the peak of each clump. Again, the background spectra were extracted from adjacent source-free regions, and the spectra were fitted with the absorbed MEKAL model. Spectra and best-fit models are shown in Figure 5. The best-fit temperatures, obtained by fixing the N_H absorption to the Galactic value and the metal abundance to the canonical value of 0.3 solar, are $6.3^{+2.2}_{-1.3}$ keV for the northeastern clump and $5.7^{+2.8}_{-1.6}$ keV for the southwestern clump (Table 5). If the abundance is left free, the gas temperatures do not change significantly. At the 90% confidence level, the temperatures of the two clumps are consistent with each other. The unabsorbed 2–10 keV flux of the northeastern and southwestern clumps is $8.8^{+0.9}_{-1.0} \times 10^{-14}$ ergs cm^{-2} s^{-1} (61% ± 7% of the entire cluster) and $5.2^{+0.9}_{-0.8} \times 10^{-14}$ ergs cm^{-2} s^{-1}, respectively.

3.3. Radial Surface Brightness Profiles

Using the 0.3–10 keV image corrected with a weighted exposure map, we extracted the azimuthally averaged radial

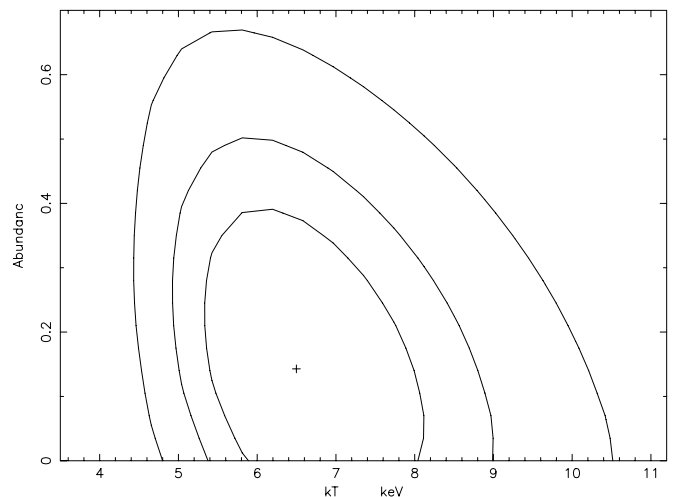Fig. 3.—Observed unfolded X-ray spectrum and the best-fit model for the entire cluster.

Fig. 4.—Confidence contours (68.3%, 90%, and 99%) from a spectral fit to the entire cluster as a function of gas temperature and metal abundance.

TABLE 4

GAS, TEMPERATURE, AND METAL ABUNDANCE MEASUREMENTS FOR THE ENTIRE CLUSTER

Observations	Temperature (keV)	Metallicity ($Z_\odot$)	χ^2/dof	Ref.
Chandra	$6.2^{+1.6}_{-1.1}$	0.3 (fixed)	78.6/76	
Chandra	$6.5^{+1.7}_{-1.3}$	$0.14^{+0.27}_{-0.14}$	77.6/75	
ROSAT.............................	6	...	...	1
BeppoSAX.........................	$6.46^{+1.74}_{-1.19}$	$0.53^{+0.29}_{-0.24}$	16.6/21	1
SZ-effect...........................	$8.7^{+4.1}_{-1.8}$	...	...	2
Chandra[n]	$5.5^{+0.9}_{-0.8}$	0.3(fixed)	...	3
Chandra[n]	$5.6^{+1.0}_{-0.8}$	$0.15^{+0.22}_{-0.15}$	32.4/36	3
Chandra[s]	$5.2^{+1.1}_{-0.9}$	0.3 (fixed)	...	3
Chandra[s]	$4.8^{+1.4}_{-0.9}$	$0.70^{+0.72}_{-0.44}$	24.5/35	3

NOTE.—Superscript [n]: northeastern clump; [s]: southwestern clump.
REFERENCES.—(1) Della Ceca et al. 2000; (2) Joy et al. 2001; (3) Maughan et al. 2003.

surface brightness profiles of the two clumps separately. Embedded pointlike sources were masked out and the background was also fitted in this procedure.

β-model.—First we attempt to describe the surface brightness profiles with a single β-model, which takes the form

$$S(r) = S_0[1 + (r/r_c)^2]^{-3\beta+0.5} + S_B, \qquad (1)$$

where r_c is the core radius, β is the index parameter, S_B is the background, and S_0 is the normalization. The best-fit

FIG. 5.—Observed unfolded X-ray spectra and the best-fit models for the northeastern and southwestern clumps.

models together with the observed profiles are shown in Figure 6 and Table 6. We find that the surface brightness profiles of the outer regions of the two clumps can be well fitted with the β-model. In the central (<30 kpc) regions, however, the observed profiles are underestimated. The calculated reduced χ^2 is 1.36 for the northeastern clump and 1.22 for the southwestern clump. Also, we find that the northeastern clump has a larger core radius than the southwestern clump.

We have tried to improve the fit of the central regions of the two clumps, where a surface brightness excess is visible, by adding a second β-model. Such a method has been successfully applied for example in "cooling flow" clusters. The poor statistics in our case, however, prevent us from constraining the additional parameters of the double β-model.

NFW-like model.—An alternative way to compensate for the central brightness excess is to utilize models that are more centrally concentrated than the β-model. To this aim, we have fitted the observed surface brightness profiles with the model expected for the gas distribution following an NFW-like halo profile as suggested in cosmological *N*-body simulations (Navarro, Frenk, & White 1995). In this case, the gas distribution has an analytic form of (Makino, Sasaki, & Suto 1998; Wu 2000)

$$\tilde{n}_{gas}(x) = \frac{(1+x)^{\alpha/x} - 1}{e^\alpha - 1}, \qquad (2)$$

which, in order to avoid the divergence in the computation of X-ray surface brightness, has been normalized so that $\tilde{n}_{gas}(x) \equiv [n_{gas}(x) - n_{gas(\infty)}]/[n_{gas}(0) - n_{gas}(\infty)]$, where $x = R/r_s$, $\alpha = 4\pi G\mu m_p \rho_s r_s^2/kT$, $\mu = 0.59$ is the average molecular weight, and ρ_s and r_s are the characteristic density and length, respectively. The surface brightness profile can correspondingly be calculated in term of $S(x) \propto \int_x^\infty \tilde{n}_{gas}^2(x)\, dl$,
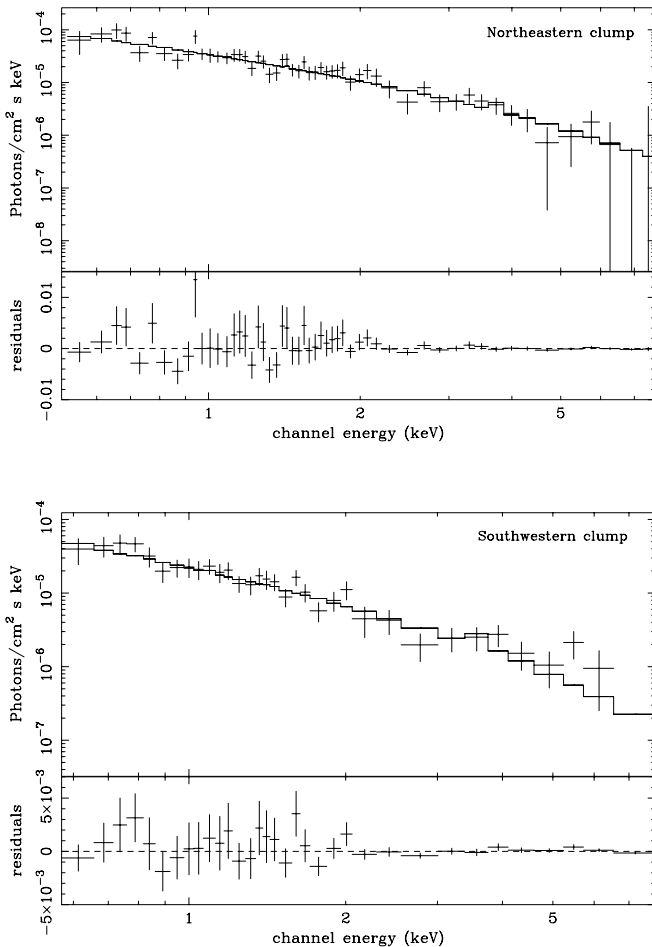
TABLE 5

GAS, TEMPERATURES, AND METAL ABUNDANCES OF THE TWO CLUMPS

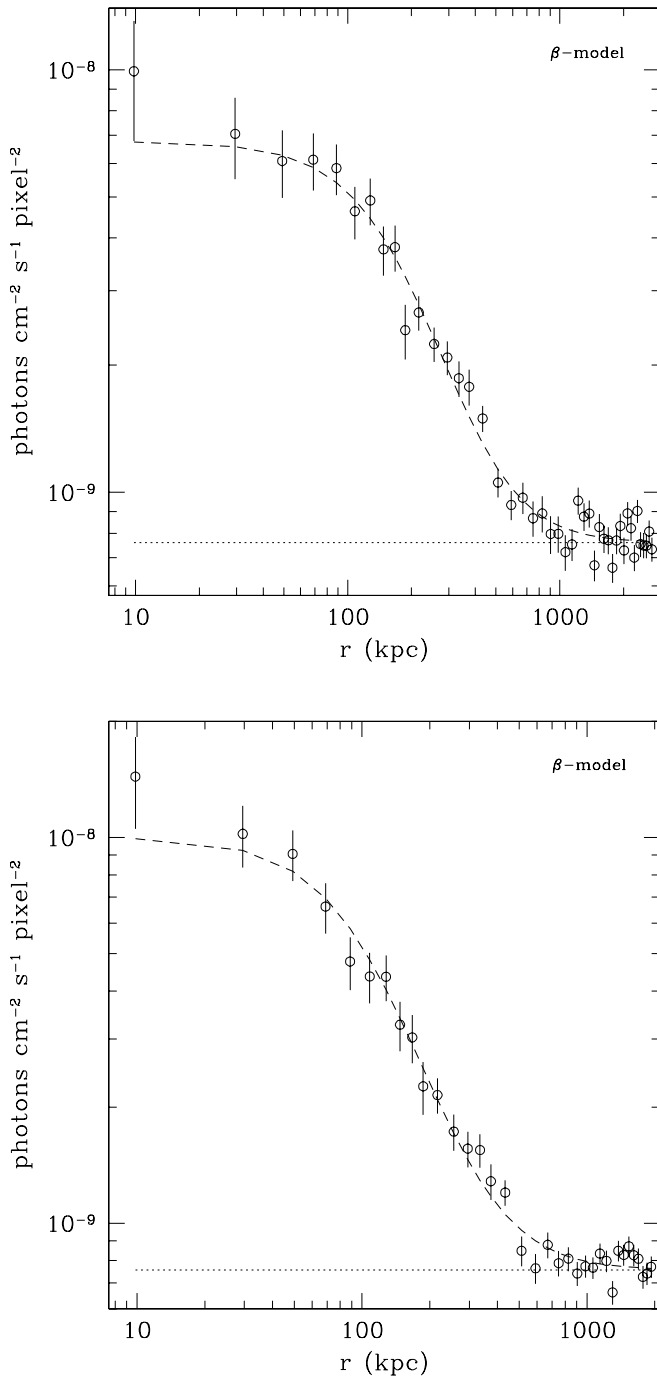| Clumps	Temperature (keV)	Metallicity ($Z_\odot$)	χ^2/dof
Northeastern clump......	$6.3^{+2.2}_{-1.3}$	0.3 (fixed)	43.6/52
	$6.6^{+2.4}_{-1.5}$	$0.16^{+0.36}_{-0.16}$	43.2/51
Southwestern clump.....	$5.7^{+2.8}_{-1.6}$	0.3 (fixed)	28.0/32
	$5.7^{+2.9}_{-1.6}$	$0.31^{+0.55}_{-0.31}$	28.0/31

FIG. 6.—Observed radial surface brightness profiles (*open circle*) and the best-fit β-model (*dashed line*) for the northeastern clump (*top*) and southwestern clump (*bottom*). The best-fit background is represented by the dotted line.

where the integral is performed along the line of sight. This yields

$$
S(x) = -S_0 \int_{x_0}^{\infty} \frac{\sqrt{x^2 + x_0^2}}{x} [(1+x)^{\alpha/x} - 1](1+x)^{\alpha/x}
$$

$$
\times \left[\frac{1}{1+x} - \frac{\ln(1+x)}{x} \right] dx + S_B, \qquad (3)
$$

where $x_0 = r/r_s$ is the dimensionless radius.

The best-fit surface brightness profiles predicted by the NFW-like model are presented in Figure 7 and Table 6. The calculated reduced χ^2 is 1.59 for the northeastern clump and 1.46 for the southwestern clump. It appears that the NFW-like model does not give a better global fit to the surface brightness profiles of the two clumps; however, it does improve the fit to the central regions.

3.4. *X-Ray Mass Determinations*

With the information obtained with the X-ray data, we have estimated the gravitational mass of Cl J0152.7−1357 in three ways. First, we calculate the virial mass of the cluster by using the cosmic virial theorem (Bryan & Norman 1998)

$$
kT = \frac{GM^{2/3}\mu m_p}{2\beta} \left[\frac{H^2(z)\Delta_c}{2G} \right]^{1/3}
$$

$$
= 1.39 f_T \left(\frac{M}{10^{15} \, M_\odot} \right)^{2/3} (h^2 \Delta_c E^2)^{1/3} \text{ keV}, \qquad (4)
$$

where the normalization factor is $f_T = 0.8$, the overdensity parameter is $\Delta_c = 200$, and $E(z) = h(1 + z)\{\Omega_M z + 1 + \Omega_\Lambda[(1 + z)^{-2} - 1]\}^{1/2}$. Because the *Chandra* temperature of the whole cluster is $6.5^{+1.7}_{-1.3}$ keV, the calculated virial mass is $9.18^{+3.82}_{-2.61} \times 10^{14} \, M_\odot$.

Second, we calculate the mass distribution by assuming that the cluster is in hydrostatic equilibrium and the gas is isothermal. In this case the total mass within a radius R can be expressed as

$$
M_\beta(R) = -\frac{kTR^2}{G\mu m_p n(R)} \frac{dn(R)}{dR}, \qquad (5)
$$

where $n(R)$ is the electron number density that can be inferred from the observed surface brightness profile with the best-fit β-model. The calculated radial mass distribution for the two clumps is shown in Figure 8.

The third way to determine the mass distribution is to employ the universal NFW profile. In this case we have

$$
M_{\mathrm{NFW}}(R) = 4\pi \rho_s R_s^3 \left[\ln\left(1 + \frac{R}{R_s}\right) - \frac{R}{R + R_s} \right]. \qquad (6)
$$

The derived mass profiles of the two clumps are also shown in Figure 8. It turns out that the latter two methods give essentially the same mass estimates except for the central regions, which may be caused by the failure of the hydrostatic equilibrium assumption in the core of the cluster or by departure from the isothermality assumption adopted in the β-model.

4. ANALYSIS OF THE OPTICAL DATA

4.1. *Mass Determinations*

Mass determinations from weak gravitational lensing analyses are considered necessarily lower estimates on the true mass of the system. In contrast with X-ray estimates, gravitational lensing offers a method for measuring projected cluster masses that is essentially free from assumptions on the dynamical state of the gravitating matter. The observed shear is unperturbed by the addition of constant density sheets along the line of sight (e.g., Gorenstein, Shapiro, & Falco 1988). Furthermore, the relatively small field of view of these

TABLE 6
Best Fits to the Surface Brightness Profiles with a β-Model and an NFW-like Model

Model	Parameters	Northeastern Clump	Southwestern Clump
β-model............................	$S_0{}^{\mathrm{a}}$	$(6.01 \pm 0.40) \times 10^{-9}$	$(9.25 \pm 0.72) \times 10^{-9}$
	r_c (arcsec)	24.05 ± 1.09	13.90 ± 0.70
	β	0.61 ± 0.02	0.58 ± 0.02
	$S_B{}^{\mathrm{a}}$	$(7.61 \pm 0.18) \times 10^{-10}$	$(7.56 \pm 0.19) \times 10^{-10}$
	χ^2/dof	55.68/41	37.67/31
NFW-like model	$S_0{}^{\mathrm{a}}$	$2.50^{+0.36}_{-0.21} \times 10^{-12}$	$4.90^{+0.64}_{-0.60} \times 10^{-12}$
	r_s (arcsec)	$37.50^{+4.26}_{-2.24}$	$19.34^{+2.17}_{-1.46}$
	α	$6.11^{+0.13}_{-0.07}$	$6.11^{+0.10}_{-0.13}$
	$S_B{}^{\mathrm{a}}$	$7.11^{+0.30}_{-0.31} \times 10^{-10}$	$6.91^{+0.35}_{-0.31} \times 10^{-10}$
	χ^2/dof	65.10/41	45.23/31

$^{\mathrm{a}}$ In units of photons cm^{-2} s^{-1} pixel^{-2}.

observations necessitates a differential determination of the total mass. This is facilitated by the statistic (Fahlman et al. 1994; Kaiser, Squires, & Broadhurst 1995)

$$\zeta(\theta_1, \theta_2) = 2(1 - \theta_1^2/\theta_2^2)^{-1} \int_{\theta_1}^{\theta_2} d\ln(\theta)\langle\gamma_t\rangle,$$
$$= \bar{\kappa}(\theta_1) - \bar{\kappa}(\theta_1 < \theta < \theta_2), \qquad (7)$$

which measures the mean dimensionless surface density $\bar{\kappa}$, interior to θ_1 relative to the mean in an annulus $\theta_1 < \theta < \theta_2$, and depends only on the measured galaxy shear estimates γ. To convert this to physical units (e.g., total mass), we estimated the angular diameter distances factored into the dimensionless surface density using HDF N+S photometric redshifts (Gwyn & Hartwick 1996; Gwyn 1999[5]).

In Figure 9 we present the radial lensing mass profile for Cl J0152.7−1357. The central point for the profile was chosen to be the point midway between the peaks of the X-ray emission (and the main optical concentrations of the cluster galaxies). For comparison purposes, we compute the mass profile for a singular isothermal sphere (SIS), $\rho \propto r^{-2}$, with the normalization set from the local T_X-σ relation (Holden et al. 2003). For the observed temperature of $T_X \simeq 6.5$ keV, this yields $\sigma \simeq 1000$ km s^{-1}. The prediction from this model is shown as the solid line in Figure 9, where we have corrected for the mass in the control annulus to enable a fair comparison with the lensing results. For $r \gtrsim 0.5 h_{0.65}^{-1}$ Mpc, the SIS model matches the data fairly well. However, at smaller radii it tends to overpredict the observed mass profile. In an attempt to improve the model, we introduced a large core in the density profile, with a softening radius of $20''$, similar to the distance from the central point to the peaks of the X-ray emission/optical concentrations of cluster galaxies. The softened model matches the observations much better at small radii.

Mass estimates based on weak lensing techniques are differential and hence tend to underestimate the total mass. By making a model-dependent assumption on the form of the total mass profile, we can correct for the mass in the control annulus and extrapolate the mass to some fiducial radius, thus providing an estimate of the mass interior to that radius. In Figure 10 we plot the estimate for the projected mass within

$1 h_{0.65}^{-1}$ Mpc, where the correction and extrapolation are calculated from the radii in Figure 9.

4.2. Light Distribution

To determine the cluster light distribution, we proceeded as follows: we obtained redshifts for 15 cluster members at Keck in 1998 November. These galaxies form a tight locus in either a $V-I$ versus $R-I$ or $V-I$ versus $V-R$ color-color plot. Using the observed colors for the spectroscopically confirmed cluster members as a guide, we identified additional cluster galaxy candidates as those galaxies having similar colors, yielding a catalog containing a total of 210 galaxies. The measured R-band magnitudes were used to estimate the cluster luminosity as

$$L_B = 10^{0.4[M_{B,\odot} - R - \langle B-R \rangle_0 + \mathrm{DM} + K(R)]} L_{B,\odot}, \qquad (8)$$

where $M_{B,\odot} = 5.48$ is the solar absolute B magnitude, DM $= 43.71$ is the distance modulus, $\langle B-R \rangle_0 = 1.81$ is the mean color of early type galaxies at $z = 0$, and $K(R) = 1.75$ is the K-correction (Coleman, Wu, & Weedman 1980).

We estimated the cluster zero-redshift mass-to-light ratio by calculating Σ_L as the mean projected luminosity density at any radius relative to the mean in the control annulus outside that radius (where zero-redshift mass-to-light ratio means that the colors of early-type galaxies at $z = 0$ were used). We then estimated $M/L = \Sigma/\Sigma_L$, which under the assumption that mass traces light, forms an unbiased estimate of the cluster light distribution (even if the cluster extends into the control annulus). The results are shown in Figure 11.

5. DISCUSSION

5.1. Cooling Time

In the central regions of the clusters where the gas density is high, the ICM will lose most of its thermal energy radiatively in a relatively short time in the absence of effective heating sources. By using the best-fit surface brightness profiles for the two clumps of Cl J0152.7−1357, we estimated their cooling time with the following analytic expression:

$$t_{\mathrm{cool}} = 2.21 \times 10^{10} \left(\frac{g}{1.2} \right)^{-1} \left(\frac{kT}{1~\mathrm{keV}} \right)^{1/2}$$
$$\times \left(\frac{n_e}{10^{-3}~\mathrm{cm}^{-3}} \right)^{-1} \mathrm{yr}, \qquad (9)$$

where g is the so-called Gaunt factor. The result is shown in Figure 12, where the maximum cooling regions are marked by setting the cooling time equal to the age of the universe. The
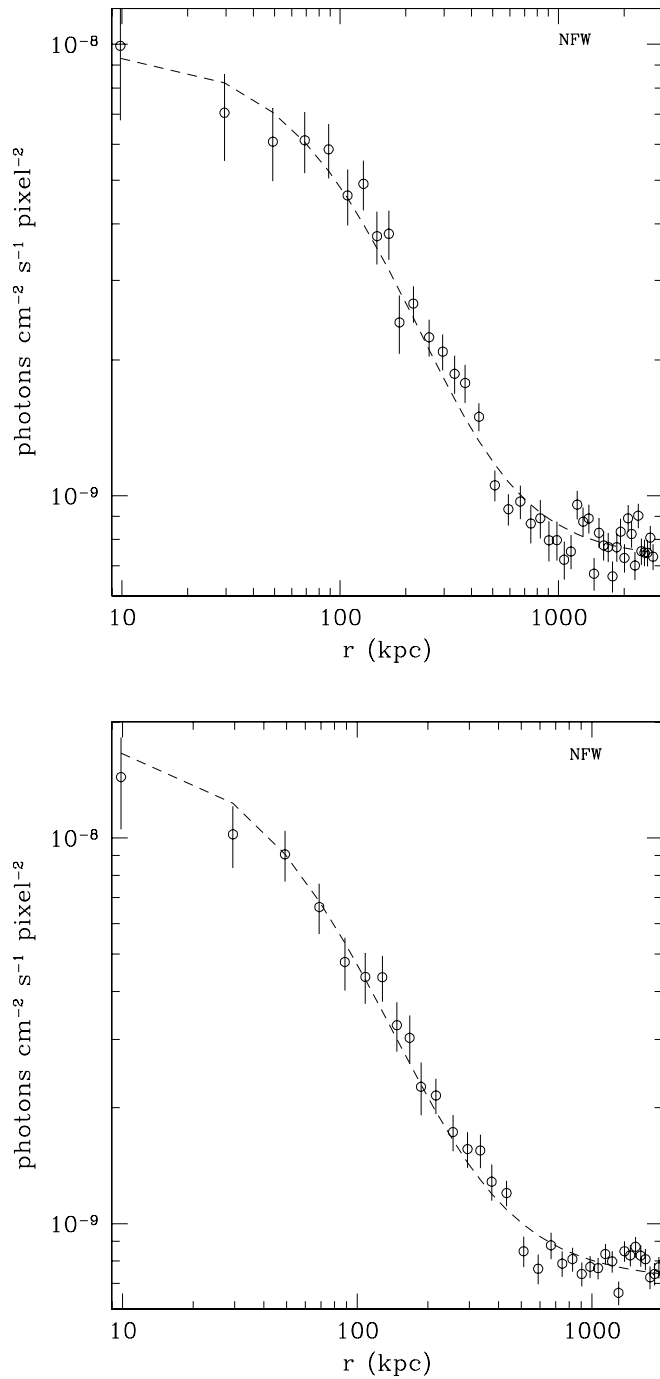
---

[5] Available at http://astrowww.phys.uvic.ca/grads/gwyn/pz/index.html.

and r_c are not available, we assume $\beta = \frac{2}{3}$ and $r_c = 0.1$ Mpc. For comparison, we also plot the *BeppoSAX* result for Cl J0152.7−1357 (D00). It appears that our measured luminosity and temperature for Cl J0152.7−1357 are consistent with the nonevolutionary scenario of the L_X-T_X relation, in keeping with the results of Maughan et al. (2003).

Given the mass profile of a galaxy cluster, its virial mass can be determined by using the characteristic radius r_{200}, within which the mean mass density is 200 times the current critical density of the universe. The calculated virial mass of Cl J0152.7−1357 $(9.99^{+2.46}_{-1.25} \times 10^{14}\ M_\odot)$ is plotted against

FIG. 7.—Observed radial surface brightness profiles (*open circle*) and the best-fit model using an NFW-like profile (*dashed line*) for the northeastern clump (*top*) and southwestern clump (*bottom*).

cooling radius is 150 kpc for the northeastern clump and 168 kpc for the southwestern clump.

5.2. *Luminosity-Temperature and Mass-Temperature Relations*

We have compared our results for Cl J0152.7−1357 with the well-defined statistical scaling relations for galaxy clusters. In Figure 13 we plot the observed L_X-T_X relation for high-redshift clusters ($z > 0.7$; Holden et al. 2002) and the best-fit L_X-T_X relation for nearby clusters (Xue & Wu 2000). Here the X-ray luminosity is calculated by integrating within r_{200}, assuming a β-model distribution. When the model parameters β

FIG. 8.—Radial mass profiles of the two clumps obtained with the best-fit β-model (*squares*) and NFW-like profile (*down triangles*).
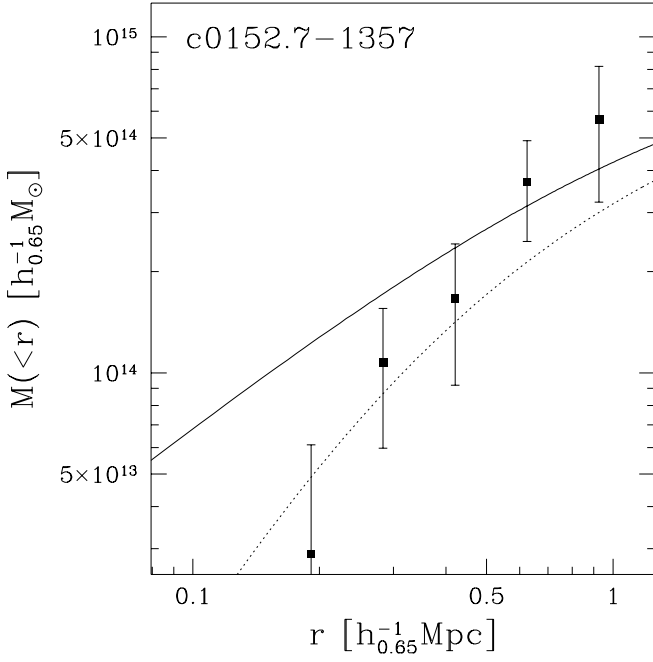
FIG. 9.—Cumulative mass profile (*data points*) for the whole cluster based on the lensing inversion technique. The solid line represents the prediction for a singular isothermal sphere model, where the normalization has been set to the local X-ray temperature/velocity dispersion relation, and assumes that the mass distribution extends into the control region. The effect of substructure was modeled by modifying the isothermal sphere to include a core radius of $20''$ (*dashed line*), where the core radius was chosen to match the angular separation of the peaks of the X-ray emission and optical centroids of the cluster galaxy concentrations.
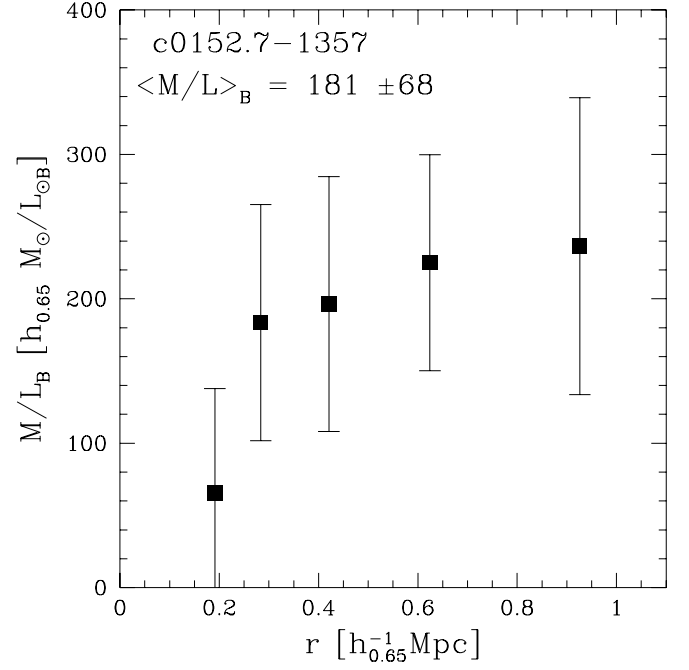
FIG. 11.—Zero-redshift mass-to-light ratio. The cluster light distribution was determined by choosing galaxies with colors similar to 15 spectroscopically confirmed cluster galaxies ($0.86 < V-R < 1.75$ and $2.40 < V-I < 3.39$). The mass-to-light ratio was taken as the ratio of the radial mean surface mass density to the projected luminosity density, relative to the mean in the circular control region outside that radius. Under the assumption that mass traces light, this forms an unbiased estimate of the cluster light distribution (even if the cluster extends into the control annulus).
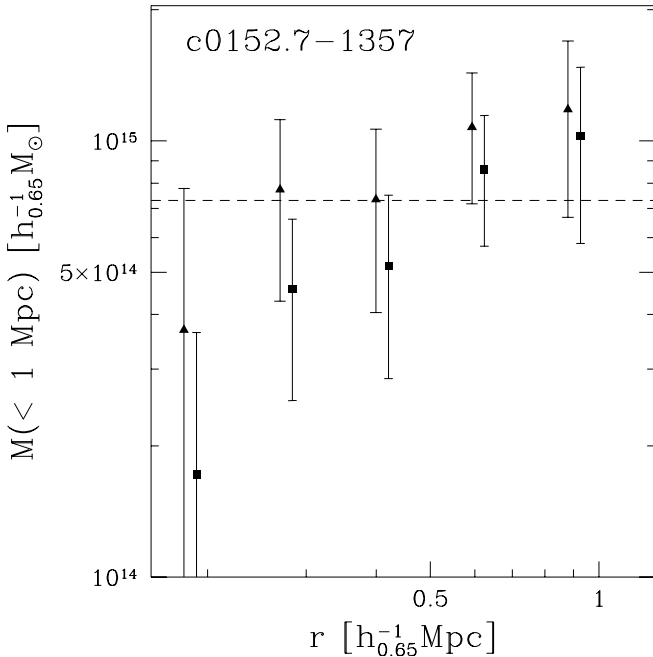
FIG. 10.—Projected cluster mass within $r = 1\,h_{0.65}^{-1}$ Mpc, as estimated from the weak lensing analysis at various radii. The dashed line is a prediction for a singular isothermal sphere normalized using the cluster X-ray temperature.
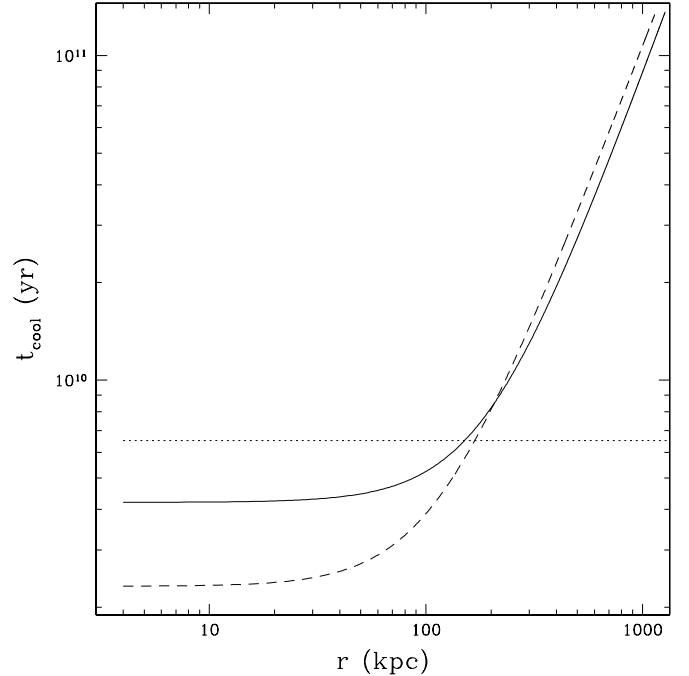

FIG. 12.—Cooling time profiles for the northeastern clump (*solid line*) and the southwestern clump (*dashed line*). The dotted line represents the age of the universe at the cluster redshift.

the X-ray temperature in Figure 14, along with the mass-temperature relation of nearby clusters (Xu, Jin, & Wu 2001). It is apparent that the mass and temperature of Cl J0152.7−1357 obtained with the *Chandra* data agree well with the relation based on the study of nearby clusters. These findings agree with those of Maughan et al. (2003), where the authors compared the mass and temperature of the two subclumps with those of the local sample (Sanderson et al. 2003) and an intermediate-redshift sample (Allen, Schmidt, & Fabian (2001).

6. SUMMARY

We have analyzed *Chandra* and Keck telescope observations of the high-redshift cluster Cl J0152.7−1357 ($z \simeq 0.83$). A complex substructure with two significant concentrations is well defined in both the X-ray and optical data. The peaks of the galaxy distribution do not coincide precisely with the X-ray emission peaks. This suggests that the cluster is not in dynamical equilibrium and may be undergoing a merger event. The X-ray temperature of the entire cluster is found to be $6.5^{+1.7}_{-1.3}$ keV, which is consistent with the results of the previous *BeppoSAX* observations ($6.46^{+1.74}_{-1.19}$ keV; D00) and Sunyaev-Zeldovich effect measurements ($8.7^{+4.1}_{-1.8}$ keV; Joy et al. 2001).

By measuring the gas temperature and X-ray surface brightness profiles, we have calculated the radial distributions of dynamical mass for the two clumps in Cl J0152.7−1357 using both the β-model and the NFW-like model. Except for the central regions of the two clumps, the two methods yield mass estimates that are consistent at the 90% confidence level. In the central regions of the two clumps, the difference between the predictions of the two methods may be due to a departure from of the hydrostatic equilibrium assumption or to the inaccuracy of the β-model and the isothermality assumption.

FIG. 14.—Mass-temperature relation for nearby clusters (*open circles*; Xu, Jin, & Wu 2001) and our *Chandra* result for Cl J0152.7−1357 (*filled circles*).

Using deep-imaging data taken with the LRIS camera at the Keck telescope, we have obtained an independent mass estimate based on a weak gravitational lensing analysis. The mass profile is consistent with that obtained from SIS model at large radii, and it is consistent with the softened model prediction at small radii. We have compared the physical properties of Cl J0152.7−1357 with those of other clusters in the literature across a large redshift range by investigating their X-ray mass-temperature and luminosity-temperature relations. In both cases we find no departure from the well-defined correlation relations at low redshift. Assuming that this cluster is representative of the general galaxy cluster population, we conclude that there is no significant evolution of the dynamical properties for clusters out to $z \approx 0.8$.
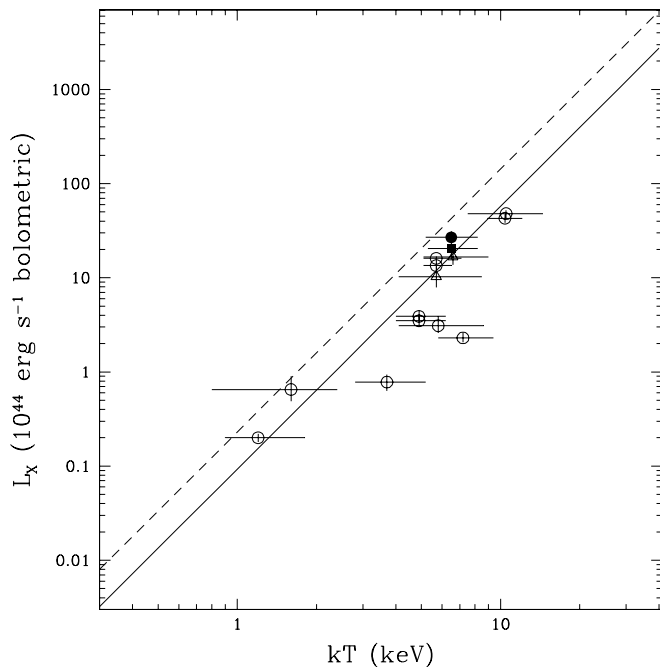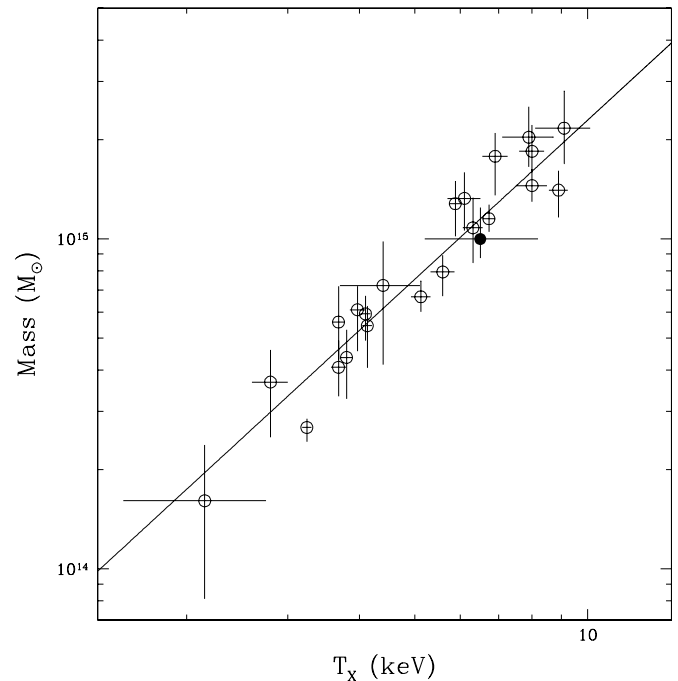

FIG. 13.—Luminosity-temperature relation for galaxy clusters. *Open circles*: Distant clusters and groups at $z > 0.7$ (Holden et al. 2002). *Filled square*: *BeppoSAX* measurements of Cl J0152.7−1357 (D00). *Triangles*: *Chandra* measurements of the two subclumps of Cl J0152.7−1357. *Filled circle*: *Chandra* measurement of the entire cluster. *Solid line*: Luminosity-temperature relation for nearby clusters (Xue & Wu 2000). *Dashed line*: Predicted evolving L_X-T relation with $(1 + z)^{1.5}$ scaling.

REFERENCES

Allen, S. W., Schmidt, R. W., & Fabian, A. C. 2001, MNRAS, 328, L37
Arnaud, K. A. 1996, in ASP Conf. Ser. 101, Astronomical Data Analysis Software and Systems V, ed. G. Jacoby & J. Barnes (San Francisco: ASP), 17
Bahcall, N. A., & Cen, R. 1992, ApJ, 398, L81
Bryan, G. L., & Norman, M. L. 1998, ApJ, 495, 80
Coleman, G. D., Wu, C.-C., & Weedman, D. W. 1980, ApJS, 43, 393
Della Ceca, R., Scaramella, R., Gioia, I. M., Rosati, P., Fiore, F., & Squires, G. 2000, A&A, 353, 498 (D00)
Dickey, J. M., & Lockman, F. J. 1990, ARA&A, 28, 215
Ebeling, H., et al. 2000, ApJ, 534, 133
Fahlman, G., Kaiser, N., Squires, G., & Woods, D. 1994, ApJ, 437, 56
Gorenstein, M. V., Shapiro, I. I., & Falco, E. E. 1988, ApJ, 327, 693
Gwyn, S. D. J. 1999, in ASP Conf. Ser. 191, Photometric Redshifts and the Detection of High Redshift Galaxies, ed. R. Weymann, L. Storrie-Lombardi, M. Sawicki, & R. Brunner (San Francisco: ASP), 61
Gwyn, S. D. J., & Hartwick, F. D. A. 1996, ApJ, 468, L77
Haiman, Z., Mohr, J. J., & Holder, G. P. 2001, ApJ, 553, 545
Hoekstra, H., Kuijken, H., Franx, M., & Squires, G. 1998, ApJ, 504, 636
Holden, B. P., Stanford, S. A., Rosati, P., Eisenhardt, P., & Tozzi, P. 2003, in Clusters of Galaxies: Probes of Cosmological Structure and Galaxy Evolution, ed. J. S. Mulchaey, A. Dressler, & A. Oemler (Pasadena: Carnegie Obs.)
Holden, B. P., Stanford, S. A., Squires, G. K., Rosati, P., Tozzi, P., Eisenhardt, P., & Spinrad, H. 2002, AJ, 124, 33

Joy, M., et al. 2001, ApJ, 551, L1
Kaiser, N. 2000, ApJ, 537, 555
Kaiser, N., & Squires, G. 1993, ApJ, 404, 441
Kaiser, N., Squires, G., & Broadhurst, T. 1995, ApJ, 449, 460 (KSB)
Kuijken, K. 1999, A&A, 352, 355
Luppino, G. A., & Kaiser, N. 1997, ApJ, 475, 20
Makino, N., Sasaki, S., & Suto, Y. 1998, ApJ, 497, 555
Maughan, B. J., Jones, L. R., Ebeling, H., Perlman, E., Rosati, P., Frye, C., & Mullis, C. R. 2003, ApJ, 587, 589
Navarro, J. F., Frenk, C. S., & White, S. D. M. 1995, MNRAS, 275, 720
Oke, J. B., et al. 1995, PASP, 107, 375
Oukbir, J., & Blanchard, A. 1997, A&A, 317, 1
Romer, A. K., et al. 2000, ApJS, 126, 209
Rosati, P., Della Ceca, R., Burg, R., Norman, C., & Giacconi, R. 1995, ApJ, 445, L11
Rosati, P., Della Ceca, R., Norman, C., & Giacconi, R. 1998, ApJ, 492, L21
Sanderson, A. J. R., Ponman, T. J., Finoguenov, A., Lloyd-Davies, E. L., & Markevitch, M. 2003, MNRAS, 340, 989
Tyson, J., Valdes, F., & Wenk, R. 1990, ApJ, 349, L1
Wu, X.-P. 2000, MNRAS, 316, 299
Xu, H.-G., Jin, G.-X., & Wu, X.-P. 2001, ApJ, 553, 78
Xue, Y.-J., & Wu, X.-P. 2000, ApJ, 538, 65